Carbon 192 (2022) 462–472

Contents lists available at ScienceDirect

Carbon

journal homepage: www.elsevier.com/locate/carbon

The structural modification and magnetism of many-layer epitaxial graphene implanted with low-energy light ions

Alessandro R. Mazza [a, b], Anna Miettinen [c], Zheng Gai [d], Xiaoqing He [e, f], Timothy R. Charlton [g], Thomas Z. Ward [b], Matthew Conrad [c], Guang Bian [a], Edward H. Conrad [c], Paul F. Miceli [a, *]

[a] Department of Physics and Astronomy, University of Missouri, Columbia, MO, USA
[b] Materials Science and Technology Division, Oak Ridge National Laboratory, Oak Ridge, TN, USA
[c] School of Physics, Georgia Institute of Technology, Atlanta, GA, USA
[d] Center for Nanophase Materials Sciences, Oak Ridge National Laboratory, Oak Ridge, TN, USA
[e] Electron Microscopy Core, University of Missouri, Columbia, MO, USA
[f] Department of Mechanical and Aerospace Engineering, University of Missouri, Columbia, MO, USA
[g] Spallation Neutron Source, Oak Ridge National Laboratory, Oak Ridge, TN, USA

ARTICLE INFO

Article history:
Received 15 December 2021
Received in revised form
13 February 2022
Accepted 21 February 2022
Available online 25 February 2022

ABSTRACT

Modifying the properties of graphene has gained wide interest for a plethora of potential applications, including spintronics. One approach has demonstrated that proton irradiation can induce ferromagnetism in graphene as well as in graphite. However, little is known about how the protons interact with graphene, the mechanism that creates the ferromagnetism, or whether the protons remain in the graphene. Here we report an investigation, broadly relevant to graphitic carbon, using low-energy (360–2000 eV) ions of hydrogen, deuterium, and helium implanted into multilayer epitaxial graphene. Complementary x-ray and neutron reflectivity demonstrate that essentially all of the implanted hydrogen remains chemisorbed in graphene. In situ x-ray diffraction reveals significantly different rates of interlayer expansion of the multilayer graphene. Analysis of these data demonstrates that the interlayer expansion arises entirely from the interstitials created by the ions and not from hydrogen that remains in the graphene. The results also establish a quantitative measure of the layer expansion due to carbon interstitials. Magnetometry and x-ray diffraction studies show that the magnetic moment relates to the amount of interstitial carbon rather than the amount of hydrogen, demonstrating that the induced room-temperature ferromagnetism arises directly from the disrupted bonding of the carbon lattice.

1. Introduction

Graphite is widely used in a myriad of applications, ranging from nuclear reactors to dry lubricants, electrical contacts, and batteries [1–6]. On a smaller scale, a single atomic layer of graphite – graphene – exhibits novel electronic properties due to its linearly dispersing bands and high electron mobility [7,8]. Its discovery has spawned nearly two decades of graphene research and, more recently, is the foundation for the study of a broad class of two-dimensional (2D) materials having weak van der Waals interlayer interactions [9–13].

As a single atomic layer, graphene is extraordinarily sensitive to its environment, which allows its properties to be modified, and many routes to its functionalization have been explored [14–17]. One such example is the attachment of H to the graphene sheet that opens a band gap and induces ferromagnetism [18,19]. This unusual p-orbital magnetism in carbon is itself interesting. The origin of magnetism in graphene is discussed in terms of defects that lead to an inequivalence among the two lattice sites in its bipartite lattice [20,21]. In highly-controlled experiments, scanning-tunneling spectroscopy measurements have revealed the electronic and magnetic properties of a single vacancy defect and of a single H atom on the surface of graphene – both cases lead to a local magnetic moment [18,22,23].

While the attachment of H to graphene surfaces has been demonstrated, its stability is fragile [24–27]. It is necessary to split

* Corresponding author.
E-mail address: micelip@missouri.edu (P.F. Miceli).

https://doi.org/10.1016/j.carbon.2022.02.046

the H_2 molecule into atomic H in order for it to stick to the graphene surface and this has been accomplished by using a hot filament [19], plasmas [24,25], and chemical synthesis [28]. However, each of these methods is limited to the exposed surface area of the graphene samples and cannot be used to uniformly dope layered graphene systems [29]. Attempts to introduce atomic H and D in between the graphene layers of epitaxial multilayer graphene, where the attached hydrogen would be protected, have shown that it does not enter in between the layers: it resides only on the surface and possibly at defect sites within the film [30]. Nevertheless, because single layers of graphene are difficult to handle, multiple layers of graphene may be more suitable for device applications, particularly epitaxial multilayer graphene.

As an alternative route to incorporating H, proton implantation at high (MeV) kinetic energies into graphite has been shown to produce ferromagnetism at room temperature [31–33]. These studies clearly demonstrate that proton irradiation induces ferromagnetism in graphite, although, many fundamental questions remain to be answered. For example, it is not known how much of the H remains in the graphite nor whether the remaining hydrogen is atomic or molecular. How does the H interact with the carbon and what role does it play in causing the magnetism? X-ray magnetic circular dichroism (XMCD) studies have suggested that H might contribute to the magnetic moment, although there are a number of assumptions necessary to model the data [34,35]. In contrast, electron spin resonance (ESR) measurements seem to conflict with this result, providing negative evidence for hydrogen playing a role in ferromagnetism in graphite which points out the clear importance of understanding the hydrogen defect density and relationship with arising magnetism [33]. A similar conclusion is found in implanted C_{60} samples, where the resulting magnetism did not to appear to correlated with implanted protons [36]. More broadly, ion implantation in MoS_2 [37] also exhibits induced ferromagnetism, suggesting a implantation might provide a general route to ferromagnetism in 2D materials.

Understanding ion interactions with graphite is also broadly important. Early studies of ion implanted graphite were driven by nuclear power applications. These primarily focused on graphite's mechanical and thermal properties as well as the aim of understanding how proton implantation leads to graphite damage and hydrogen uptake [38–46]. For example, an interlayer expansion and a decrease in the crystalline size of graphite as a result of H and He ion implantation is observed from transition electron microscopy (TEM) studies [44–46]. Hydrogen recombination into H_2 is believed to, in part, drive the change in graphite crystal size, although, experimental corroboration of hydrogen's exact role has yet to be understood.

Rather than use high-energy ions, a potentially more useful approach for studying ion implantation in graphitic carbon would be to investigate atomically thin graphene samples with low-energy (hundreds of eV) ions, which allows more quantitative studies for obtaining fundamental information while still being able to modify the graphene lattice [47]. This approach also caters to device fabrication by utilizing the unique properties of graphene along with the potential for ion beam patterning to create regions of functionalized/doped graphene. For example, very low energy ions of B, N, and C were shown to modify the electrical properties of graphene, including switching the sign of the magnetoresistance [48,49]. It is noted that ion beams can be controlled with high resolution (sub-nm) [50] and a potentially useful technological pathway could be the use of ion beams to write onto graphene and other 2D materials. Since the layers are very thin, it can be done at low energies with nanoscale depth control using readily available laboratory tools.

In this paper, we investigate how low-energy H, D, and He ions affect the structure of multilayer graphene grown epitaxially on C-face 4H–SiC and we relate the results to the induced ferromagnetism that is observed. The high sample quality of thin and atomically-flat epitaxial graphene layers is key to enabling quantitative studies. Complementary neutron and x-ray reflectivity is used to determine the amount of hydrogen that remains after implantation. X-ray diffraction measured in situ during implantation determined the interlayer expansion as a function of the ion dose. These results show that the expansion caused by different species of ions can be quantitatively related to the interstitials created. Low-energy ions allow nanoscale control of the implantation depth and our investigation reveals the existence of two different implantation regimes, depending on whether the average ion range resides within the film or at the buried interface. We show how x-ray diffraction measurements can distinguish these regimes and their resulting differences with respect to ion damage. It is also shown that H is chemisorbed to the carbon. From magnetometry measurements as a function of H dose, which is combined with x-ray diffraction measurements, we show that the induced ferromagnetism is directly related to carbon interstitial formation and not the H chemisorption. These results provide important insight into how low-energy ions modify multilayer graphene and, more broadly, graphitic carbon; thereby, opening the door to potential ion-beam writing for the nanoscale manipulation of graphene layers and other 2D materials.

2. Experimental

2.1. Sample growth

The graphene samples were grown on $(000\bar{1})$ (C-face) of 4H–SiC 9×9 mm wafers from Cree, Inc. Multilayer epitaxial graphene is obtained using the pre-treatment and confinement-controlled sublimation (CCS) process described by de Heer et al. [51]. To grow samples exceeding 10 graphene layers additional growth cycles, usually 4 or 5, were needed in order to achieve 30+ graphene layers. The growth cycles allow for the cleaning of excess Si on the graphite crucible that is used to control the Si vapor pressure and the graphene growth rate.

2.2. Implantation performed in-situ with X-ray diffraction

At low energy, the range and the distribution of ions within the multilayer epitaxial graphene can be controlled on the nanoscale. Consequently, we investigated two qualitatively different ion distributions, one with the average ion range in the center of the graphene layer and one with the average range at the buried interface, between the graphene and the SiC. Examples of these distributions are shown in Fig. 1. Ion distributions were calculated using SRIM (described below and in the supplementary materials) and, in this way, the ion energy could be chosen for a given graphene thickness in order to achieve the desired ion distribution. A complete list of all samples studied is given in Table 1. The sample naming convention gives information about the location of the center of the ion distribution (Int or Gr for interface of graphene/SiC or graphene respectively), the ion type (hydrogen, H, deuterium, D, or helium, He), and the thickness (number of layers). The thickness of all samples is determined by x-ray reflectivity.

X-ray diffraction data was collected in situ, at various ion doses, for samples H-Gr-60, H-Int-78, D-Int-20 and D-Int-22 and He-Int-30. Implantation is accomplished using a Phi ion gun where 10^{-5} Torr of H_2, D_2 or He gas is admitted into a vacuum chamber,

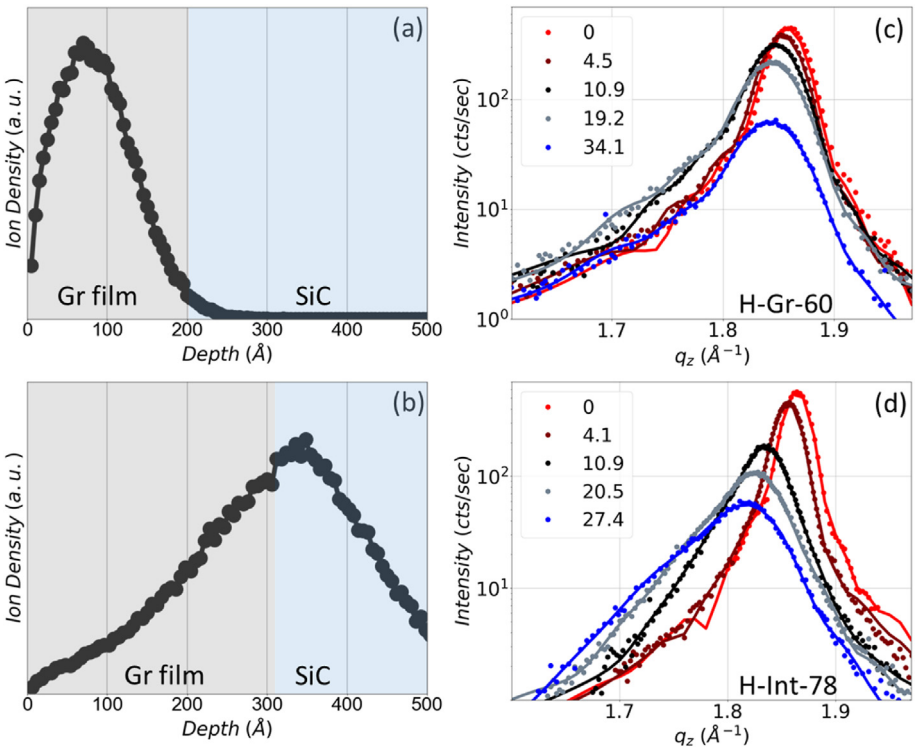

Fig. 1. Ion distributions for samples H-Gr-60 (a) and H-Gr-78 (b) calculated from SRIM demonstrating the location of ions relative to the buried interface of graphene/SiC. Also shown is the x-ray diffraction data measured in situ for different ion fluences during the implantation of (c) H-Gr-60 and (d) H-Int-78. The key gives the proton fluence in units of 10^{16} ions/cm^2. The solid curves are best fits to the model described in the supplement. It can be seen that the graphene layer spacing progressively expands with increasing ion fluence. (A colour version of this figure can be viewed online.)

base pressure 10^{-10} Torr. The ion flux is determined for each implantation condition: 3 ± 1.5 μA/cm^2 for 2 kV acceleration voltage, 1.5 ± 0.7 μA/cm^2 for 1 kV, and 1.1 ± 0.6 μA/cm^2 for 500 V. These experiments were carried out to high fluences until very high strain or limited change was observed in the x-ray diffraction with increased ion fluence.

A multilayer focusing elliptical mirror monochromator was used to focus CuK-alpha from a rotating anode x-ray generator in point-focus geometry into the vacuum chamber with a beam size of 1×1mm. In-situ extended range x-ray reflectivity (EXRR) data was collected as a function of ion dose for the first order graphene Bragg reflection. Data was collected immediately following ion implantation for each of the reported fluences. Sample alignment did not change during the duration of the experiment allowing for reliable comparison of sample (001) reflection intensity and position. Data was collected with the scattering vector along the surface normal, with wavevector transfer $q_z = 4\pi/\lambda \sin(2\theta/2)$, where λ is the x-ray wavelength.

Sample H-Gr-50 was measured *ex-situ* using a four-circle high-resolution x-ray diffractometer (X'Pert Pro, Panalytical with CuKα_1 radiation) after each dose where it was implanted with an ion flux of 0.3 ± 0.05 μA/cm^2 for 360 V acceleration voltage.

2.3. SRIM calculations

The ion distribution in the samples is estimated using SRIM software [52] which calculates the approximate path of implanted ions of a given incident energy for an amorphous sample having a given density and composition. SRIM directly outputs the final ion distribution as well as the final target atom distribution, which results from target atoms moved from their original location. For the calculations given here (performed for 10^6 incident ions), SiC is assumed to have a density of 3.211 g/cm^3 and graphene a density of 2.2 g/cm^3. The ion and atom distributions are given in units of number density/fluence.

2.4. Neutron reflectivity (NR)

NR data was obtained on the reflectometer, BL-4A, at the Spallation Neutron Source (SNS) at Oak Ridge National Laboratory. Data was collected on a two-dimensional position sensitive detector at room temperature. The data were then reduced by integrating a region of interest on the detector along $q_{||} = 0$ and subtracting a neighboring parallel region of interest in order to produce the specular line. Data is fit using the Refl1D [53]. X-ray reflectivity (XRR) was measured using a rotating anode x-ray generator with a flat Ge(111) monochromator that produced a high-resolution MoKα1 beam having a horizontal angular divergence of 0.003 degrees. Due to the neutron sensitivity to hydrogen, complementary measurements of NR and XRR provide a robust method of determining hydrogen content in implanted graphene samples.

2.5. X-ray photoelectron spectroscopy (XPS)

XPS was run on a SIGMA PULSE system which utilizes MECS monochromator (quartz crystal mirror for the Bragg reflection) and focusing of Al-Kα radiation on a Rowland circle with 500 mm diameter. This allows for high-resolution measurements which can be run *in-situ* during sample annealing. The sample environment was in UHV, with a sample stage which allows for annealing to nominally 800–900 K. A single sample, D-Int-22, was studied after D ion implantation. The sample was studied before annealing, during (*in-situ*) annealing, and after the annealing process was finished. For comparison, an untreated sample was also run under

the same conditions.

2.6. Magnetic properties measurements

Magnetization measurements were conducted on a Quantum Design MPMS3 magnetometer and are corrected for substrate background by subtracting the diamagnetic background signal from collected data. The diamagnetic signal is subtracted by measuring a bare SiC substrate at the appropriate temperature and directly subtracting (corrected for sample mass) the substrate signal. In order to reduce the impact of handling the samples, the magnetization was measured only with the field applied in-plane.

3. Results

3.1. Graphene layer expansion due to ion implantation

In situ x-ray diffraction measurements of the graphene (001) Bragg reflection, which corresponds to the interlayer distance between the graphene sheets, d, are shown for different H-ion fluences in Fig. 1. The average ion range is located within the graphene film in Fig. 1(c) whereas it is located at the buried interface in Fig. 1(d) as is evident from their respective calculated ion profiles in Fig. 1(a) and (b) respectively. Although the line shapes viewed on a logarithmic intensity scale exhibit slight differences for the two ion distributions – a point addressed quantitatively in the supplement – it can be seen that in both cases the Bragg reflection progressively moves to lower q_z with increasing fluence, indicating that the spacing between the graphene layers, d, increases with fluence. All samples studied, with different thicknesses, ion types and ion distributions, exhibit this behavior.

The effect of the increasing interlayer expansion with dose for all samples is captured in Fig. 2(a) which shows the relative layer expansion, $\varepsilon = \frac{\delta d}{d}$, determined from the center-of-mass position of the Bragg reflection. The dose is given as an average ion density within the graphene, which is obtained from SRIM calculations performed for each sample using the experimental conditions and the ion fluence (details in the supplement). As can be seen, there are considerable differences among the expansion curves for the different samples and ion types. A common feature of these data, however, is that the expansion begins to saturate as the ion density approaches the carbon density. We have modeled (solid curves in Fig. 2(a)) these data according to,

$$\varepsilon = \varepsilon^{sat}\left(1 - e^{-kc}\right) \quad (1$$

where c is the average ion density, k is a parameter related to the ion density at which the strain begins to saturate, and ε^{sat} is the saturation value of the interlayer expansion. The two parameters, k and ε^{sat}, were fit to the data and the results are given in Table 2. It can be seen that the k values are similar among all of the samples, indicating a similar saturation ion density in each case. This point is highlighted in Fig. 2(b), which divides the measured expansion by ε^{sat} to demonstrate that the saturation occurs as the ion density approaches the carbon density. Fig. 2(b) also illustrates that the essential differences among *all* of the data can be described by a *single* parameter in the model: the saturation value of the interlayer expansion, ε^{sat}.

The large differences among the data in Fig. 2(a) suggest that the implanted ions themselves might not be directly responsible for the observed expansion. In particular, we note that He causes the largest expansion although this inert atom is not expected to chemically bind to the carbon in order to expand the graphene layers. We have, therefore, explored the role of carbon interstitials.

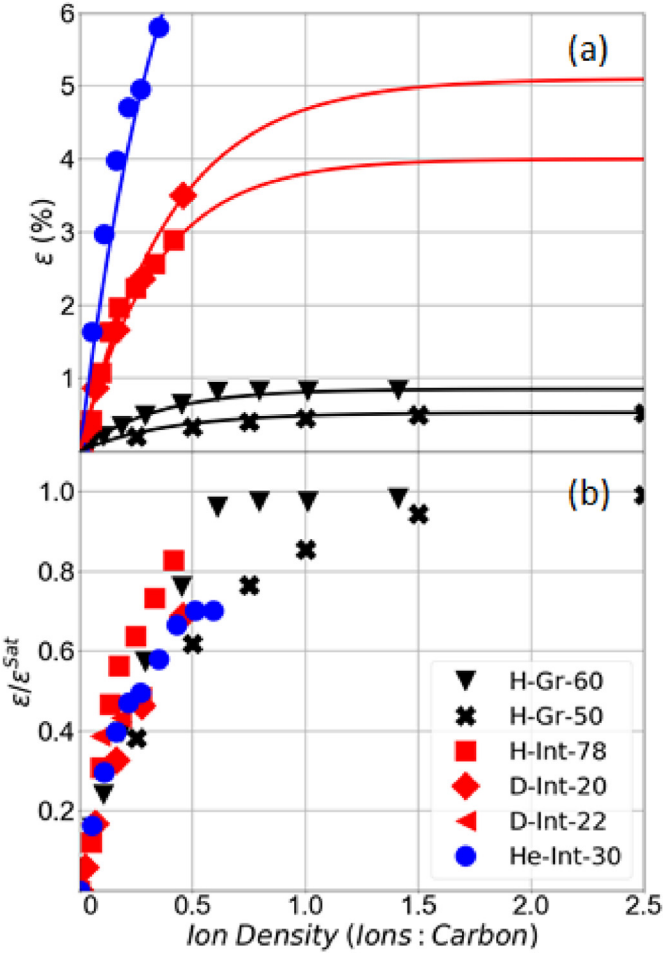

Fig. 2. (a) shows the graphene interlayer expansion vs. ion density (dose) for samples implanted with hydrogen, deuterium, and helium. The solid curves are the best fit to the data using eq. (1) described in the text. In (b), the data in (a) are normalized by the maximum expansion, ε^{sat}, obtained from the fitted curves in (a). The plot demonstrates that the interlayer expansion begins to saturate for all samples as the ion density approaches the carbon density. Sample D-Int-22 is included to show repeatability, but implantation was not carried out to high ion density and therefore was unable to be fit. (A colour version of this figure can be viewed online.)

From SRIM, we have determined the number of carbon interstitials generated in the graphene layer for the experimental conditions of each sample (see supplemental materials). These calculations allow us to determine the average number of carbon interstitials generated in the graphene per incident ion , β, for each ion energy, ion type, and for each of the sample's thickness parameters. The result of these calculations for β are given in Table 2.

We can show that the experimentally observed interlayer expansion is entirely due to the carbon interstitials created by the ions. Because ε^{sat} is the single model parameter that reflects the expansion in each sample, we have plotted it versus β in Fig. 3 for each sample studied. As can be seen, there is a striking linear dependence on β. Note that this simple relationship occurs despite the fact that the interstitials were generated by a broad range of experimental conditions, which include three types of ions, different ion energies and different graphene film thicknesses.

It can also be shown that the expansion depends linearly on the carbon interstitial density n, when the density is low, as would be expected if the interstitials cause the expansion. Fig. 4 shows the low-n region of the data in Fig. 2(a) replotted by converting the ion density to the interstitial density, $n = \beta c$. The expansion data

Table 1
Samples used in this study.

Sample	Thickness (Layers)	Ion Energy (eV)	Ion Type	Total Fluence (10^{16}ions/cm^2)	Distribution Center
H-Gr-60	60	500	H	34.1	Graphene
H-Gr-50	50	360	H	46.8	Graphene
H-Int-78	78	2000	H	27.4	Interface
H-Int-23	23	500	H	85.8	Interface
H-Int-21	21	500	H	28.6	Interface
D-Int-20	20	500	D	12.8	Interface
D-Int-22	22	500	D	3.8	Interface
He-Int-30	30	1000	He	14.1	Interface

Table 2
Parameters obtained by fitting the dose-dependent data in Fig. 2(a) to eq. (1). β, the number of carbon interstitials produced per ion, was calculated for each sample using SRIM.

Sample	ε_{Sat}	k	β (Interstitials/ion)
H-Gr-60	0.85	3	0.97
H-Gr-50	0.53	2.5	0.44
H-Int-78	4	3	4.82
D-Int-20	5.1	2.5	4.91
He-Int-30	10	2.5	14.04

clearly exhibits a linear dependence on the interstitial density, $\varepsilon = (\delta v)n$, for all samples at low interstitial density. The data also exhibits the same slope, δv=0.2 Å^3, which is obtained from a fit to the data of all samples in Fig. 4. This result should be contrasted with the varying slopes at low ion density observed in Fig. 2(a): replotting versus the carbon interstitial density reveals an expansion with the same slope for all of the data, thereby making it clear that the expansion, prior to saturation, derives from interstitials and not ions. It is worth emphasizing that the controlled geometry of these experiments, where we use an epitaxial graphene film having nanoscale thickness rather than a macroscopic sample of graphite, is a key experimental strategy that enables a quantitative determination of the basic expansion mechanism due to low-energy ions in graphitic materials.

3.2. Hydrogen retention

We turn now to the question of whether the implanted H ions remain in the sample or if they escape. Grazing-angle neutron reflectivity (NR), which is sensitive to the hydrogen density due to the neutron's negative coherent scattering length for H, is used in conjunction with grazing-angle x-ray reflectivity (XRR) to determine both the layer structure and the hydrogen retention of an implanted sample. This negative scattering length of H reflects our decision to study H and not D implanted samples, as it provides the clearest contrast in comparison to un-implanted samples. Neutrons scatter from nuclei whereas x-rays scatter from electrons, yielding a significantly different elemental contrast for the two probes. Since scattering at grazing angles is sensitive to the nanometer scale (rather than the atomic scale), the data are modeled in terms of several layers having an average scattering length density (SLD) [53]. We co-refined both the neutron and x-ray reflectivity data using the same structural model so that the combined results produce a higher confidence for the modeled parameters, including the hydrogen content.

Fig. 5(a) and (b) show the x-ray and neutron reflectivity results, respectively, for a H-implanted sample, H-Int-78. XRR is also measured prior to implantation. In a prior investigation of un-implanted many-layer graphene on C-face 4H SiC it is found that a 3-layer model is required to accommodate the rough buried interface between graphene and SiC [54]. These three layers are comprised of the graphene layer, a transition (T) layer between

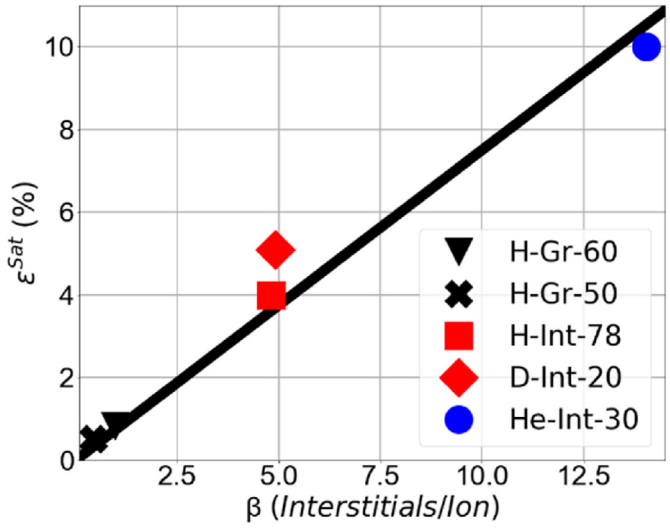

Fig. 3. demonstrates a linear relationship between the saturation interlayer expansion, ε^{sat}, which was obtained from fitting the data in Fig. 2(a), and the number of carbon interstitials generated per ion. The solid line is fit to the data which has a slope of 0.75% expansion per interstitials/ion. This result shows that the interlayer expansion of graphene is due to carbon interstitials, independent of the type of ion, the ion range or ion energy. (A colour version of this figure can be viewed online.)

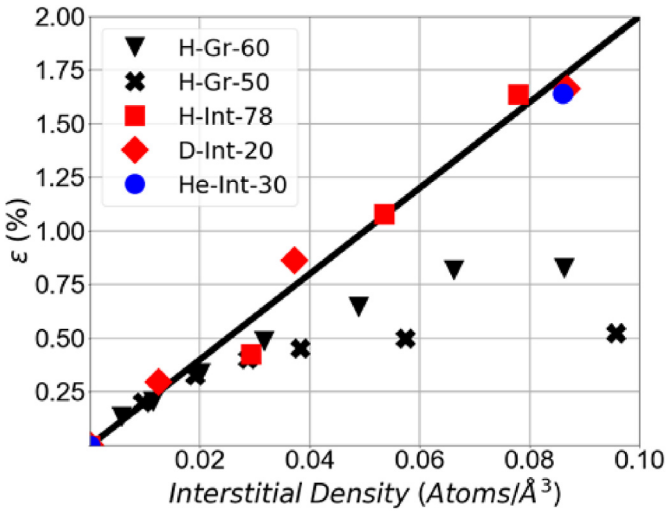

Fig. 4. shows the interlayer expansion plotted versus the calculated interstitial density in the low-density region of the data for samples implanted with hydrogen, deuterium, and helium. The solid line, with a slope of 0.2 Å^3, demonstrates that all samples exhibit the same slope at low density, indicating that the interstitials are the source of the expansion. (A colour version of this figure can be viewed online.)

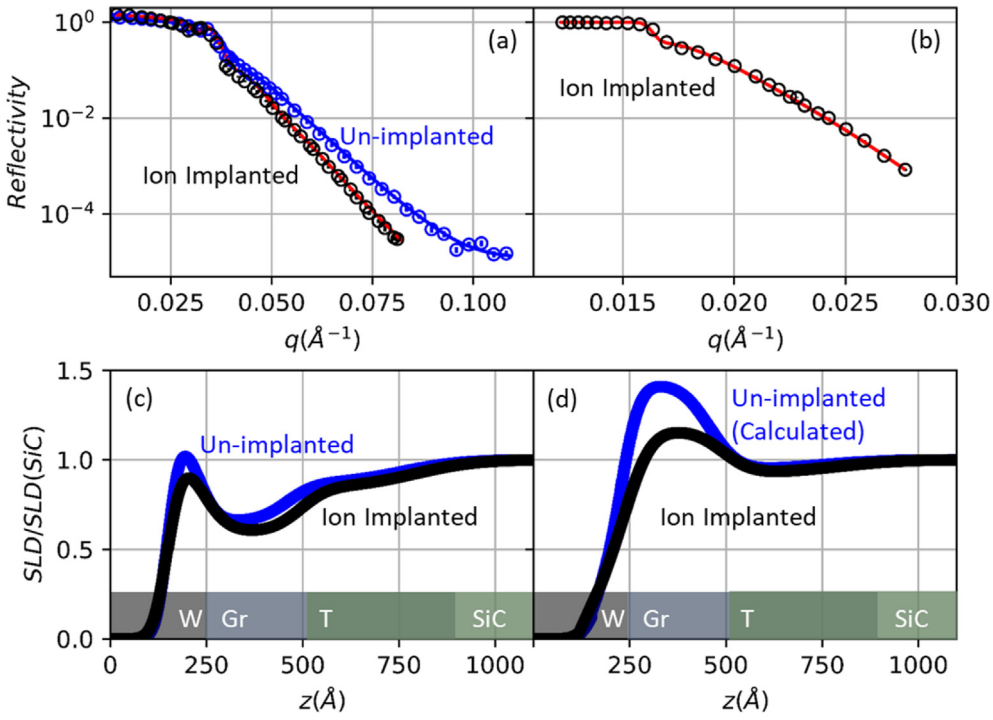

Fig. 5. (a) XRR for the un-implanted and the H implanted sample. (b) NR for the implanted sample. The data (symbols) were taken on the same sample, H-Int-78. The solid curves show the fitted model, which is discussed in the text. (c) Shows the resulting SLD profile that was obtained from fitting the XRR data in (a) for both the un-implanted and implanted sample. (d) Shows the SLD profile obtained from fitting the NR data of the implanted sample as well as the neutron SLD for the un-implanted sample calculated from the measured XRR. The color bands at the bottom of (c) and (d) indicate the layers assumed in the model, as discussed in the text. (A colour version of this figure can be viewed online.)

graphene/SiC accommodating the rough interface, and the SiC substrate. In addition to these layers, H-Int-78 has a thin tungsten (W) layer on the surface from exposure to a tungsten filament in vacuum. It influences the reflectivity profile shape, and the W layer is included in the XRR/NR co-refinement by adding a 4th top-layer to the model. The layer structure is schematically indicated by colored bands at the bottom of Fig. 5 (c) and (d). The amount of W is small, with approximately 5 nm total coverage contained in islands that cover at most 20% of the surface of the sample (determined from x-ray scattering). The W layer should not affect the retention of hydrogen as the surface coverage is very small.

Because hydrogen is a negligible scatterer of x-rays, the effect of implantation does not impact the x-ray SLD of graphene other than a slight roughening of the sample, revealed by the sharper drop in reflectivity seen in Fig. 5(a) and the corresponding broadening of the graphene/SiC interface in the SLD profile in Fig. 5(c). NR, in contrast to XRR, is highly sensitive to the negative SLD of hydrogen. The effect of hydrogenation is observed by the large decrease in SLD within the "Gr" layer, which can be seen when comparing the calculated profile for the pristine sample and the profile for the implanted sample seen in Fig. 5(d). Given the effect on the SLD, the hydrogen density can be determined by requiring that the joint refinement of the x-ray and neutron SLDs arise from the same atomic number densities of carbon ρ_C and hydrogen ρ_H. The graphene SLDs are then calculated as:

$$SLD_{Neutron} = b_C^N \rho_C + b_H^N \rho_H \quad (2a$$

$$SLD_{X-ray} = b_C^X \rho_C + b_H^X \rho_H \quad (2b$$

where b_C^N and b_C^X are the scattering lengths of carbon for neutrons and x-rays, respectively, and b_H^N and b_H^X are the scattering lengths of hydrogen for neutrons and x-rays, respectively. For x-rays, the scattering length for hydrogen, b_H^X, is negligible. Our model assumes a uniform spatial distribution of hydrogen because the limited q-range of the neutron data reduces our sensitivity to a gradient. From the joint refinement of the x-ray and neutron reflectivity data, the hydrogen content in the graphene is determined to be 0.3(± 0.05) H:C which should be compared to the 0.38(± 0.04) that is determined to be in the sample from SRIM calculations considering the total measured ion dose. Therefore, we conclude that nearly all of the implanted H remains in the graphene. Due to the limited q-range of the data, we are unable to accurately determine from NR the amount of H in the SiC, which can be between 0 and 0.2 H:C in SiC. The amount of H in the graphene layer is well-determined experimentally because it strongly influences the critical angle for total reflection whereas determining the amount of H in the buried layer of SiC would require having data with a larger range in q.

Additional investigation of the retention of H ions was performed with x-ray photoelectron spectroscopy (XPS). XPS measurements were done on a deuterium-implanted sample (D-Int-22) to look for evidence of deuterium bonding to carbon. The *C1s* spectra can be compared to pristine graphene on SiC [55,56], which is primarily sp^2 with some sp^3 carbon resulting from defects. We annealed the sample for 1000s in steps of 100 °C, starting at 50 °C. For reference, the temperatures 150 °C, 250 °C, 350 °C, 450 °C and 550 °C were reached at 1000s, 2000s, 3000s, 4000s, 5000s respectively. During this time, the *C1s* peak is measured in order to investigate the relative contributions of sp^2 and sp^3 carbon. The sp^3 carbon peak occurs at higher binding energy than the sp^2 peak so that the two contributions can be distinguished by fitting the shape of the *C1s* peak.

The effect of annealing is shown in Fig. 6, with the inset illustrating the *C1s* peak before and after annealing along with the fitted components. As can be seen, the ratio of sp^2/sp^3 carbon increases as

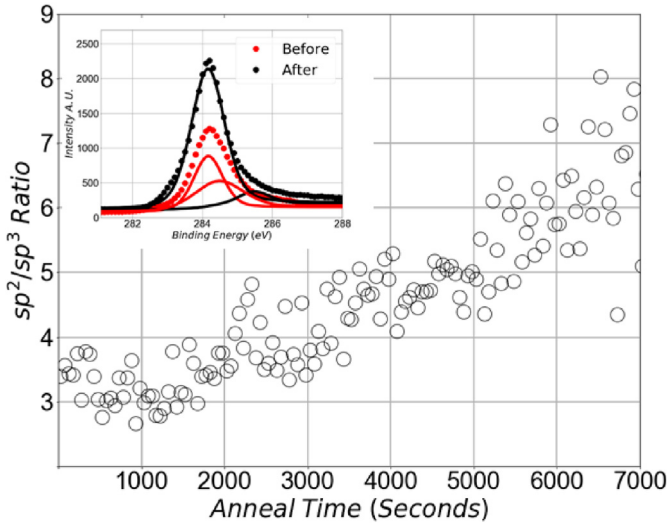

Fig. 6. The XPS area ratio of the sp^2/sp^3 carbon contributions to the C1s peak as a function of annealing time while heating to 550C. The inset shows the C1s peak before and after annealing and the solid curves show the relative sp^2 and sp^3 contributions used to fit the data. (A colour version of this figure can be viewed online.)

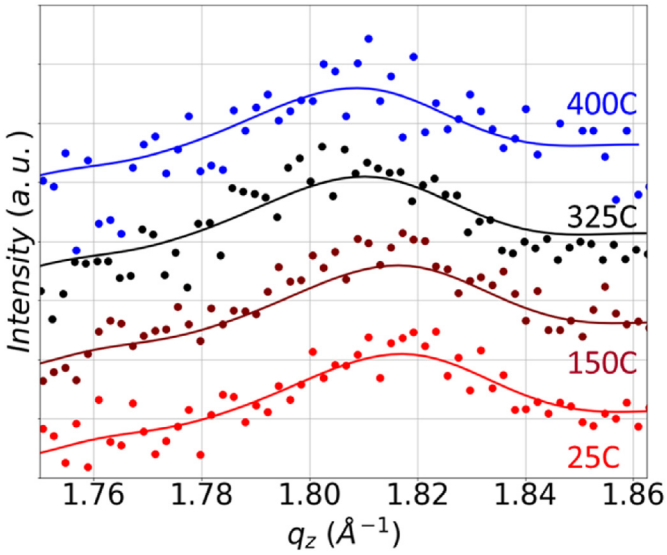

Fig. 7. The evolution of the graphene first order Bragg peak as a function of annealing temperature for a H implanted sample (H-Int-78). As can be seen, the graphene film does not recover to the un-implanted state (q_z~1.865 Å). The solid curves are a guide-to-the-eye, where a curve, fit to the dataset at 25 °C, was simply shifted to lower q_z to account for thermal expansion for each of the other temperatures. (A colour version of this figure can be viewed online.)

a function of annealing time, indicating that sp^3 carbon is being converted back to sp^2 carbon. Interestingly, the sp^2/sp^3 ratio does not saturate even at 550 °C, suggesting defects are still being annealed out even at these temperatures. This conversion does not appear to be temperature dependent, as the rate of conversion is constant upon ramping the temperature from 50 to 550 °C and it, therefore, implies that the morphology or kinetics, rather than the enthalpy, inhibit the removal of hydrogen. While the amount of sp^3 carbon cannot be determined, this result (with knowledge from NR showing H retention) indicates that graphene forms hydrocarbon bonds upon ion implantation and this conversion is reversible, contrary to sp^3 carbon-carbon bonds which are energetically much more difficult to repair via low-temperature annealing [57]. Other types of defects, such as unstable carbon adatoms and vacancies, could contribute to the reversibility of sp^2/sp^3 bonded carbon but would be impossible to distinguish from H–C bonding with XPS. However, the annealing of carbon defects would lead to reversibility of the layer expansion which, as discussed below, is not observed. Therefore, we attribute the sp^3 signal in the XPS to H–C bonds.

Although the retention of hydrogen suggests that H might be at least partly responsible for the interlayer expansion, our studies show no reversibility of the expansion when H is removed. As shown in Fig. 7, after implantation there is no significant change in position of the interlayer graphene (001) Bragg peak upon annealing to 400 °C in helium atmosphere (in order to avoid oxidation of graphene). Here the slight shift to lower q_z is due to thermal expansion, captured in the solid curves which are derived from the fits to the 25 °C data and shifted by the calculated thermal expansion of graphite. It is noted that H_2 would leave the film at these temperatures as mobility calculations and diffusion experiments show that molecular hydrogen moves rapidly both in graphene and graphite even at room temperature, making it unlikely to remain in the film after ion implantation [20,21,58]. Further, the XPS measurements of Fig. 6 indicate that implanted H, which is attached to carbon, can be removed by annealing. This result corroborates the result of the XPS annealing study, where the sample is also found to show no reversal of the interlayer expansion in ex-situ experiments. Therefore, the lack of reversibility with annealing shown in Fig. 7 indicates that H plays little role in the interlayer expansion.

We also note that the disorder introduced by the ions has a strong impact on the electronic band structure. Angle-resolved photoemission (ARPES) measured on a sample (H-Int-21) implanted with high fluence of ions (1:1 H:C ratio) with their average range at the buried interface but the data was found to be featureless, implying the ion damage has a large effect on the electronic properties. By contrast, un-implanted samples where many layers of graphene grown on C-face 4H–SiC are found to exhibit the Dirac cones that are characteristic of single layer graphene [31,54].

3.3. The effect of ion damage on the diffraction line-shape

The x-ray diffraction line-shape reveals useful information about the nature of the ion damage. When viewed on a logarithmic intensity scale, Fig. 1(c) and (d) exhibit important differences in the shape of the Bragg peak. We can accurately account for these differences by including strain and reduced crystalline size in our diffraction model, shown by the solid curves in Fig. 1. Full details of the model are given in the supplementary materials. In short, we find that a strain gradient must be used in order to explain the diffraction line-shape when the average ion range is near the buried interface, as is the case in Fig. 1(d). This gradient is reasonably expected as the density of interstitials increases from the surface towards the buried interface for this type of ion distribution. Conversely, we do not observe this gradient when the average ion range is within the film, as in Fig. 1(c). In this case, however, we find significant broadening that results from a reduced crystalline coherence, meaning that there is a broadening of the Bragg peak that cannot be explained by a strain gradient or from the film thickness, pointing to crystalline elements that are thinner than the thickness of the film. Therefore, when the average ion range is within the film, significant crystalline damage occurs such that the crystalline coherence perpendicular to the graphene layers is less than the thickness of the graphene film. It can be seen that our diffraction model, shown by the solid curves in Fig. 1, provides an excellent description of the x-ray diffraction data in both cases.

The reduced crystalline coherence that occurs when the average ion range is within the film is also manifested by rotational disorder in the graphene film. Fig. 8 shows the intensity of the specular x-ray reflection that is integrated along q_z (from data such as those shown in Fig. 1) as a function of ion fluence. The intensity is integrated using the fitted model so that all of the intensity could be captured regardless of the statistical quality in different regions of the data. In the absence of orientational disorder, intensity integrated in this manner will not change as the peak broadens along q_z. When the average ion range is centered at the buried interface, Fig. 8 shows that the integrated specular intensity barely changes with ion fluence, indicating little orientational disorder in this case. When the average ion range is centered in the graphene film, however, Fig. 8 shows an initial precipitous drop in specular intensity and then it slowly decreases with increasing fluence, indicating significant orientational disorder that develops at low fluence. Nevertheless, a significant (~25% of the sample) specular Bragg reflection persists to high fluence, indicating the persistence of graphene that maintains its initial orientation to within instrumental resolution of 0.03°. These results demonstrate that the reduced crystalline coherence occurs concomitantly with the development of orientational disorder.

3.4. Ion-induced ferromagnetism

With the understanding of how the ions influence the structure of the epitaxial graphene, we are in a position to explore the relationship between the implanted ions and the induced ferromagnetism. Several samples were measured post-implantation by magnetometry and each exhibits ferromagnetic behavior, as shown in Fig. 9. It is noted that the magnitude of the saturation moment *density* is on the order of (or larger) than those observed in bulk graphite [31,59] However, it is noted that one difficulty in estimating moment densities from the bulk graphite studies is the uncertainty of the relevant volume, which is not an issue for the epitaxial films. We observe that the ferromagnetic transition temperature is well above room temperature, evident from magnetization vs. temperature measurements shown in the supplement, Fig. S6, for samples H-Int-21 and H-Int-23. There is little difference between field-cooled (FC) and zero-field-cooled (ZFC) measurements, suggesting very small ferromagnetic domain sizes.

To explore the role of H implantation in magnetism, we investigate, with XRD and magnetometry, the same sample (H-Gr-50) as a function of dose. The experimental conditions were chosen so that the H ions were centered in the graphene in order to eliminate potential contribution of ions inducing magnetism in the SiC substrate. After each dosing, the sample was removed from the implantation chamber so that x-ray diffraction and magnetometry measurements could be performed.

The dose dependence of the saturation moment (M_S) measured at T = 300 K is shown in Fig. 10. M_S initially increases rapidly with ion dose (black circles) with the moment increasing at a much slower rate after the implanted ion density approaches the density of carbon. It is instructive to replot the saturation moment data

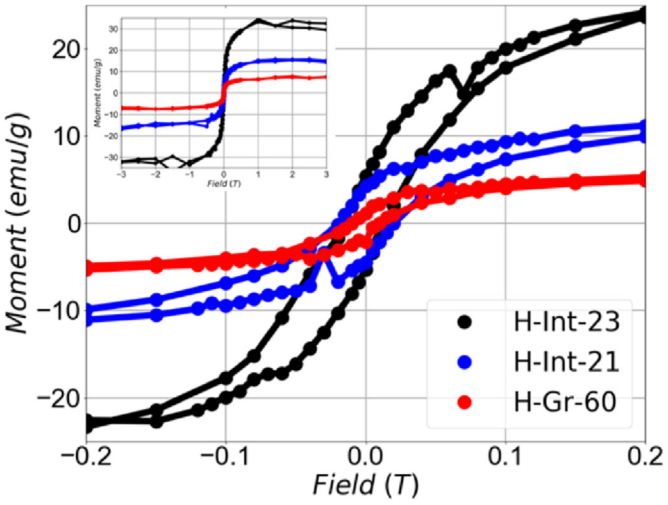

Fig. 9. Magnetization measurements at 10 K of samples measured after implantation. Samples H-Int-23 and H-Int-21 were not measured in-situ. Each sample exhibits clear remnant magnetization and has a hysteresis of ~150 Oe. (A colour version of this figure can be viewed online.)

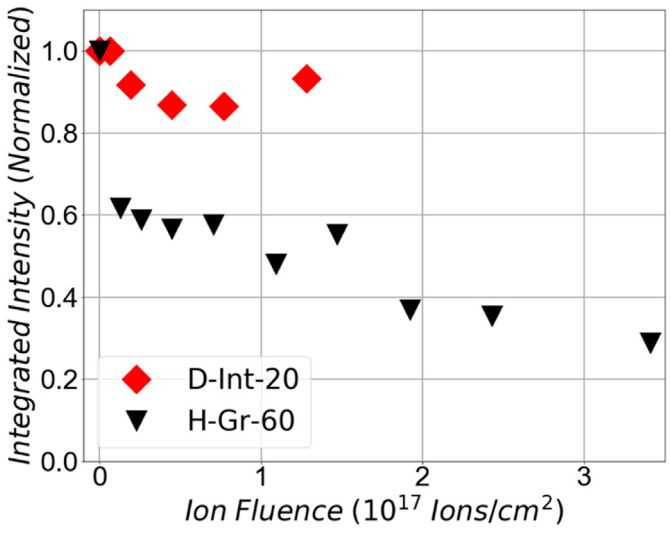

Fig. 8. The fluence-dependence of the integrated intensity of the (001) Bragg reflection normalized by the integrated intensity prior to implantation, which is shown for two samples. The case where the ion range is centered at the buried interface (D-Int-20) shows almost no decrease in integrated intensity with fluence. In contrast, when the ion range is in the graphene layer (H-Gr-60), there is an initial drop of integrated intensity followed by a slow decrease with fluence, signifying a loss of crystalline coherence of the graphene, which is consistent with our x-ray diffraction model discussed in the supplemental materials. (A colour version of this figure can be viewed online.)

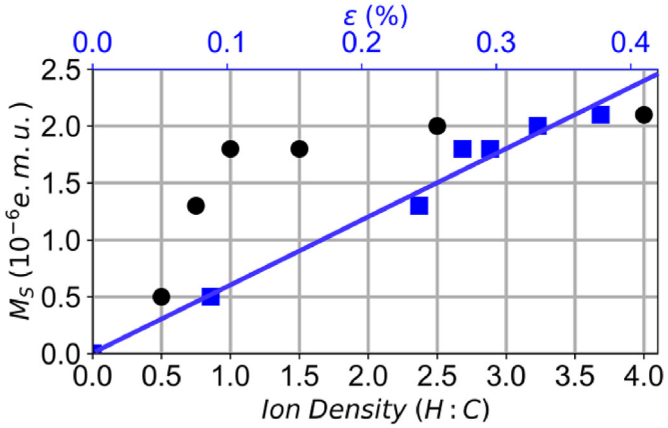

Fig. 10. The measured saturation magnetic moment (M_S) at 300 K for sample H-Gr-50 is plotted versus the implanted ion density (black circles) as well as versus the interlayer expansion of graphene (blue squares). Because we have shown that the expansion is directly related to the carbon interstitials, these data demonstrate that the magnetic moment in the sample is proportional to the carbon interstitial density. (A colour version of this figure can be viewed online.)

versus the measured interlayer expansion, which is also shown in Fig. 10. It can be seen that there is a striking linear dependence of the moment on the layer expansion. Because we have shown that the interlayer expansion is caused entirely by interstitial carbon, the results of Fig. 10 clearly demonstrate that the magnetic moment is proportional to the number of carbon interstitials. Therefore, the implanted protons induce magnetism only indirectly, through their effect of creating carbon interstitials.

4. Discussion

The geometry provided by a thin multilayer graphene film combined with the nanometer-scale controlled range of ions implanted at low energy enables a quantitative investigation of how H, D, and He ions modify graphitic carbon. We have shown that interstitials cause an expansion of the graphene layers and the strain per interstitial could be determined. The nature of the ion damage, which is revealed by the x-ray line-shapes, is observed to depend on the range of the ions. The amount of implanted hydrogen is also measured using NR, which is facilitated by the thin film geometry. It is shown that the magnetic moment arises from carbon defects and it does not scale with the amount of implanted H. As a result, the magnetic moment per interstitial carbon can be quantified because the irradiated volume is well-defined in the thin film.

Knowing the amount of H that remains implanted in the samples is an important step in understanding how the protons affect graphitic carbon. While there have been several studies using much higher proton energies implanted into bulk graphite and other layered materials [31,48], little is known about the amount of H that remains in samples, the form of the remaining H, or the nature of the damage from implantation. This is particularly true for studies of low energy ion implantation. In our work, we find that all of the implanted hydrogen remains in the graphene from NR and our XPS measurements show that a hydrocarbon-like bond is formed. Without this bonding, it would be difficult to retain all of the H in these very thin nanoscale films where H would otherwise escape. It is noted that high energy protons can form H_2 bubbles in graphite [60], which apparently does not occur in our thin films implanted with low energy protons.

Despite the presence of the hydrogen, however, the interlayer expansion between the graphene layers is shown to be entirely due to the interstitial carbon created by the ions. Indeed, He ions, which do not bind to carbon, cause a significantly larger expansion than H because He generates a larger number of interstitials per ion (β). The relationship to interstitials is quantitative, as demonstrated by Figs. 3 and 4, and the dependence of the expansion on the carbon interstitial density is shown to broadly follow the mathematical form of Eq. (1) for different ion types, ion ranges and kinetic energies.

X-ray diffraction measurements also provide insight into the crystalline damage that is caused by the ions. Because the range of low-energy ions can be tuned on the nanoscale, we could explore the effect of ion-stopping within the film. We observe distinct differences in the x-ray line-shape when the average ion range is located at the buried interface as compared to when it is within the multilayer graphene film. In the case where the ions have their average range near the buried graphene/SiC interface, we find that a linear strain gradient quantitatively describes the XRD data as a function of ion fluence. Strain gradients have been previously observed in irradiated graphite fibers, where TEM studies have shown that the gradient is due to a geometrical effect resulting from hydrocarbon bonds that increase the radius of the graphite layers [44,45]. The strain gradient in multilayer graphene, however, has a different origin as it comes from the gradient in the interstitial distribution, which increases towards the buried interface.

In contrast, when the average ion distribution is centered in the graphene film, there is no observable strain gradient. This result is not surprising because the interstitial distribution is symmetric within the film (the interstitial distribution closely follows the ion distribution; see supplement). It is noted that the magnitude of the strain for the centered ion distribution is also significantly smaller according to the data in Fig. 2, which is due, in part, to the lower kinetic energy required to place the average ion distribution in the center of the multilayer graphene film as compared to the buried interface. For example, sample H-Int-78 is only slightly thicker than H-Gr-60, but it requires more kinetic energy to place the ion distribution at the buried interface due to the direct relationship of ion range and ion energy (see supplementary materials for SRIM calculations). If the protons distributed their kinetic energy uniformly, it would amount to 17 eV/layer for H-Gr-60 and 26 eV/layer for H-Int-78 - the latter case will obviously create more interstitials. These considerations of ion energy, distribution, and type are implicitly accounted for in calculating β. Fig. 3 demonstrates that the layer expansion for all samples, regardless of the location of the ion distribution, is quantitatively explained by the number of interstitials generated per ion.

It is also apparent from x-ray diffraction that there is a pronounced loss of crystalline coherence when the ion distribution is centered in the multilayer graphene film. This observation is manifested in two independent ways: (1) modeling of the diffraction line-shape requires crystalline sizes smaller than the film thickness and (2) the specular component of the Bragg reflection decreases precipitously with fluence, indicating a strong onset of rotational disorder. Together, these observations indicate a breakup of the multilayer crystalline order into smaller crystals that also lose their initial orientational order with respect to the substrate. The reduced crystalline order results from a large number of ions that stop within the film. While these lower-energy ions are less likely to create interstitial carbon, they still have enough energy (a few eV as discussed in Ref. [47]) to break a number of carbon bonds in the vicinity where the ion stops. Previous studies of low-energy H implantation in graphite have shown irreversible and highly damaged regions that result from the clustering and recombination of ions as they stop in the sample, causing irreversible crystalline damage that can lead to both decreased crystalline size as well as exfoliation [45]. It is consistent with the crystalline damage that we see for ion distributions centered in our multilayer graphene films. We note that this loss of crystalline order is distinguished from the more point-defect-like disorder that occurs from carbon interstitials when most of the ions pass through the film, as is the case when the ion distribution is centered at the buried interface. By working with a multilayer graphene film of nanoscale thickness, rather than bulk materials, we have been able to controllably tune and interpret the two regimes of the ion-carbon interaction.

The insight from our structural investigation helps us understand the magnetism that is induced by implanted ions in multilayer graphene films. Our results clearly show that the magnetic moment is proportional to the number of carbon interstitials and not the implanted H density, demonstrating that the magnetism arises directly from the disrupted carbon bonds. This observation is consistent with a study of graphite where an induced magnetic moment is found for both implanted H and He ions, with He giving a larger moment [59,61]. In addition, these results agree with ESR measurements which propose that implanted protons do not contribute to ferromagnetism in proton implanted graphite [33]. We find that the interstitial density is significantly larger for implanted He than for H and our results quantitatively tie the magnetic moment to the interstitial density. Furthermore, the results in Fig. 9 also show that the saturation moment increases as

interstitial density increases. This is evident as the sample with the largest moment, H-Int-23, has a factor of 3 larger interstitial density than H-Int-21, a factor of 5 larger than that of H-Gr-60, and a factor of 8.5 larger than that of H-Gr-50, which is commensurate with their difference in measured moment and shows the results are universal across the measured samples. Reflecting on this point, it is insightful to discuss the role of β in creating magnetic samples. Given the direct relationship established between the saturation moment and the interstitial density in films, it is evident that by increasing β, which controls the maximum interstitial density, one can increase the maximum ferromagnetic moment achievable in graphene samples.

Although the exact nature of the disorder related to the carbon interstitials resulting from ion implantation is not known, it is expected that a range of carbon defects, including vacancies and small remnants of carbon sheets, are capable of producing magnetic moments [20,21]. Indeed, we observe a small hysteresis (~150 Oe) in the magnetization (Fig. 9), which is consistent with ferromagnetism arising from small domain sizes. Furthermore, we find little difference between field-cooled and zero-field-cooled temperature-dependent measurements (see supplement), which is consistent with small magnetic domain sizes. Therefore, we use the interstitial density, which is measurable by x-ray diffraction, as an overall gauge of the carbon disorder. With this caveat in mind, we estimate the magnetic moment per interstitial from Fig. 10 and use the relationship between the number of carbon interstitials per proton for the given experimental conditions. This analysis gives $0.03\mu_B$ per interstitial, which is significantly smaller than the theoretical maximum of 1.0–1.3 μ_B per defect [62].

The small value of the moment per interstitial suggests a low efficiency for creating magnetism. Although the ion damage disrupts the carbon bonding, it is likely that many carbon configurations involve carbon-carbon bonds that quench the p-orbital magnetic moment. Further, there is the question of the role of H, which remains in the sample. The hydrocarbon-like bonding observed in XPS might explain the presence of bonds with H that is observed in an XMCD study [34,35], although, the H contribution to the magnetic moment reported in that study is likely to be negligibly small according to our results and others [59,61]. We speculate that the H forms bonds at carbon defects and edges, thereby quenching some of the potential magnetic moments while still leaving other unpaired p-orbitals available to produce the magnetic moments.

5. Conclusions

The controlled geometry provided by epitaxial multilayer graphene grown on SiC substrates has enabled us to investigate how low-energy ions of H, D, and He modify the structure and magnetism of multilayer graphene. More generally, our results are also relevant to other forms of graphitic carbon. By combining neutron and x-ray reflectivity, we have shown that implanted hydrogen remains in the graphene. Nevertheless, in situ x-ray diffraction investigations demonstrate that the interlayer expansion of the multilayer graphene is not due to the ions that come to rest in the film; instead, it is driven solely by the carbon interstitials that are created by the implanted ions. The damage to the graphene layers also depends on the average range of the ions. When the average ion range is within the film, a relatively lower number of carbon interstitials are created while there is a significantly diminished crystalline coherence of the multilayered graphene. However, when the ion distribution is centered at the buried interface or beyond, these higher-energy ions create more carbon interstitials with a disorder that has a point-defect nature. The magnetic moment that is induced by ion implantation is clearly shown to arise from the carbon defects that are created and not from the ions themselves. This discovery unambiguously clears up the question of the origin of the magnetic moment in ion-implanted graphitic materials, as is suggested by the presence of magnetism in He irradiated graphite [59].

This investigation provides essential new insight on how low-energy ions modify both the structure and magnetism of multilayer graphene and, importantly, the results can be extended to other forms of graphitic carbon. Because low-energy ions are relatively easy to create in the laboratory, a potentially useful application could be the use of focused low-energy beams of light ions to modify films of 2D materials on the nanometer scale where one can “write” magnetic and insulating regions in proximity to regions of pristine material. This approach might provide a useful method to controllably functionalize 2D materials for technological applications.

CRediT authorship contribution statement

Alessandro R. Mazza: Investigation, Conceptualization, Methodology, Formal analysis, Writing. **Anna Miettinen:** Resources. **Zheng Gai:** Investigation. **Xiaoqing He:** Investigation. **Timothy R. Charlton:** Investigation, Methodology, Supervision. **Thomas Z. Ward:** Methodology, Supervision. **Matthew Conrad:** Resources. **Guang Bian:** Investigation. **Edward H. Conrad:** Resources. **Paul F. Miceli:** Supervision, Conceptualization, Methodology, Formal analysis, Writing.

Declaration of competing interest

The authors declare that they have no known competing financial interests or personal relationships that could have appeared to influence the work reported in this paper.

Acknowledgements

The authors would like to acknowledge the support of the National Science Foundation grant no. DGE-1069091 as well as support from the Oak Ridge National Laboratory GO! Fellowship. This material is based upon work supported by the U.S. Department of Energy, Office of Science, Office of Workforce Development for Teachers and Scientists, Office of Science Graduate Student Research (SCGSR) program. The SCGSR program is administered by the Oak Ridge Institute for Science and Education for the DOE under contract number DE-SC0014664. A portion of this research used resources at the Spallation Neutron Source, a DOE Office of Science User Facility operated by the Oak Ridge National Laboratory. A portion of this work was supported by the University of Missouri Electron Microscopy Core Excellence in Electron Microscopy award. A portion of the ion irradiation work was supported by the Department of Energy (DOE), Office of Science, Basic Energy Sciences, Materials Sciences and Engineering Division. A portion of this research was conducted at the Center for Nanophase Materials Sciences, which is a Department of Energy Office of Science User Facility.

Appendix. A Supplementary data

Supplementary data to this article can be found online at https://doi.org/10.1016/j.carbon.2022.02.046.

References

[1] J. Asenbauer, T. Eisenmann, M. Kuenzel, A. Kazzazi, Z. Chen, D. Bresser, The success story of graphite as a lithium-ion anode material – fundamentals, remaining challenges, and recent developments including silicon (oxide) composites, Sustain. Energy Fuels 4 (2020) 5387.

[2] J.D. Arregui-Mena, W. Bodel, R.N. Worth, L. Margetts, P.M. Mummery, Spatial variability in the mechanical properties of gilsocarbon, Carbon 110 (2016) 497.

[3] W.P. Eatherly, Nuclear graphite—the first years, J. Nucl. Mater. 100 (1981) 55.

[4] B.V. de Almeida, E.S. Neves, S.N. Silva, F. Vernilli Junior, Blast furnace hearth lining: post mortem analysis, Mater. Res. 20 (2017) 814.

[5] Md R. Akanda, M. Sohail, Md A. Aziz, A.-N. Kawde, Recent advances in nanomaterial-modified pencil graphite electrodes for electroanalysis, Electroanalysis 28 (2016) 408.

[6] S. Ritter, Pencil and pencil lead, Chem. Eng. News 79 (2001) 35.

[7] M.J. Allen, V.C. Tung, R.B. Kaner, Honeycomb carbon: a review of graphene, Chem. Rev. 110 (2010) 132.

[8] A.K. Geim, K.S. Novoselov, The rise of graphene, Nat. Mater. 6 (2007) 183.

[9] K.S. Novoselov, A. Mishchenko, A. Carvalho, A.H. Castro Neto, 2D materials and van Der Waals heterostructures, Science 353 (2016) aac9439.

[10] P. Ajayan, P. Kim, K. Banerjee, Two-dimensional van Der Waals materials, Phys. Today 69 (2016) 38.

[11] J.F. Sierra, J. Fabian, R.K. Kawakami, S. Roche, S.O. Valenzuela, Van der Waals heterostructures for spintronics and opto-spintronics, Nat. Nanotechnol. 16 (2021) 856.

[12] D. Rhodes, S.H. Chae, R. Ribeiro-Palau, J. Hone, Disorder in van Der Waals heterostructures of 2D materials, Nat. Mater. 18 (2019) 541.

[13] X. Guo, H. Hu, D. Hu, B. Liao, K. Chen, L. Liu, X. Zhu, X. Yang, Q. Dai, High-efficiency modulation of coupling between different polaritons in an in-plane graphene/hexagonal boron nitride heterostructure, Nanoscale 11 (2019) 2703.

[14] D. Chen, H. Feng, J. Li, Graphene oxide: preparation, functionalization, and electrochemical applications, Chem. Rev. 112 (2012) 6027.

[15] H. He, C. Gao, *Supraparamagnetic, conductive, and processable multifunctional graphene nanosheets Coated with high-density Fe_3O_4 nanoparticles*, ACS Appl. Mater. Interfaces 2 (2010) 3201.

[16] Md S. Islam, K. Ushida, S. Tanaka, T. Makino, A. Hashimoto, Effect of boron and nitrogen doping with native point defects on the vibrational properties of graphene, Comput. Mater. Sci. 94 (2014) 35.

[17] M. Pumera, C.H.A. Wong, Graphane and hydrogenated graphene, Chem. Soc. Rev. 42 (2013) 5987.

[18] H. Gonzalez-Herrero, J.M. Gomez-Rodriguez, P. Mallet, M. Moaied, J.J. Palacios, C. Salgado, M.M. Ugeda, J.-Y. Veuillen, F. Yndurain, I. Brihuega, Atomic-scale control of graphene magnetism by using hydrogen atoms, Science 352 (2016) 437.

[19] R. Balog, B. Jørgensen, J. Wells, E. Lægsgaard, P. Hofmann, F. Besenbacher, L. Hornekær, Atomic hydrogen adsorbate structures on graphene, J. Am. Chem. Soc. 131 (2009) 8744.

[20] E.H. Lieb, Two theorems on the Hubbard model, Phys. Rev. Lett. 62 (1989) 1201.

[21] O.V. Yazyev, M.I. Katsnelson, Theory of Magnetism in Graphene, in Science and Technology of Atomic, Molecular, Condensed Matter & Biological Systems, vol. 2, Elsevier, 2012, pp. 71–103.

[22] M.M. Ugeda, I. Brihuega, F. Guinea, J.M. Gómez-Rodríguez, Missing atom as a source of carbon magnetism, Phys. Rev. Lett. 104 (2010), 096804.

[23] B.R.K. Nanda, M. Sherafati, Z.S. Popović, S. Satpathy, Electronic structure of the substitutional vacancy in graphene: density-functional and green's function studies, New J. Phys. 14 (2012), 083004.

[24] Z. Luo, J. Shang, S. Lim, D. Li, Q. Xiong, Z. Shen, J. Lin, T. Yu, Modulating the electronic structures of graphene by controllable hydrogenation, Appl. Phys. Lett. 97 (2010) 233111.

[25] Z. Luo, T. Yu, K. Kim, Z. Ni, Y. You, S. Lim, Z. Shen, S. Wang, J. Lin, Thickness-dependent reversible hydrogenation of graphene layers, ACS Nano 3 (2009) 1781.

[26] K.E. Whitener, Review article: hydrogenated graphene: a user's guide, J. Vac. Sci. Technol. 36 (2018), 05G401.

[27] K.E. Whitener, W.-K. Lee, R. Stine, C.R. Tamanaha, D.A. Kidwell, J.T. Robinson, P.E. Sheehan, Activation of radical addition to graphene by chemical hydrogenation, RSC Adv. 6 (2016) 93356.

[28] A.Y.S. Eng, Z. Sofer, Š. Huber, D. Bouša, M. Maryško, M. Pumera, Hydrogenated graphenes by birch reduction: influence of electron and proton sources on hydrogenation efficiency, magnetism, and electrochemistry, Chem. Eur J. 21 (2015) 16828.

[29] R.E. Mapasha, A.M. Ukpong, N. Chetty, Ab initio *Studies of hydrogen Adatoms on bilayer graphene*, Phys. Rev. B 85 (2012) 205402.

[30] A.R. Mazza, A. Miettinen, M. Conrad, T.R. Charlton, X. He, S. Guha, G. Bian, J. Lin, E.H. Conrad, P.F. Miceli, Atomic deuteration of epitaxial many-layer graphene on 4H-SiC(0001), J. Vac. Sci. Technol. B 37 (2019), 041804.

[31] P. Esquinazi, A. Setzer, R. Höhne, C. Semmelhack, Y. Kopelevich, D. Spemann, T. Butz, B. Kohlstrunk, M. Lösche, Ferromagnetism in oriented graphite samples, Phys. Rev. B 66 (2002), 024429.

[32] P. Esquinazi, D. Spemann, R. Höhne, A. Setzer, K.-H. Han, T. Butz, Induced magnetic ordering by proton irradiation in graphite, Phys. Rev. Lett. 91 (2003) 227201.

[33] K.W. Lee, C.E. Lee, Electron spin resonance of proton-irradiated graphite, Phys. Rev. Lett. 97 (2006) 137206.

[34] H. Ohldag, T. Tyliszczak, R. Höhne, D. Spemann, P. Esquinazi, M. Ungureanu, T. Butz, π -electron ferromagnetism in metal-free carbon probed by soft X-ray dichroism, Phys. Rev. Lett. 98 (2007) 187204.

[35] H. Ohldag, P. Esquinazi, E. Arenholz, D. Spemann, M. Rothermel, A. Setzer, T. Butz, The role of hydrogen in room-temperature ferromagnetism at graphite surfaces, New J. Phys. 12 (2010) 123012.

[36] K.W. Lee, H. Kweon, C.E. Lee, Field-induced transition from room-temperature ferromagnetism to diamagnetism in proton-irradiated fullerene, Adv. Mater. 25 (2013) 5663.

[37] S. Mathew, K. Gopinadhan, T.K. Chan, X.J. Yu, D. Zhan, L. Cao, A. Rusydi, M.B.H. Breese, S. Dhar, Z.X. Shen, T. Venkatesan, J.T.L. Thong, *Magnetism in MoS_2 Induced by proton irradiation*, Appl. Phys. Lett. 101 (2012) 102103.

[38] N.J. Dutta, S.R. Mohanty, N. Buzarbaruah, Modification on graphite due to helium ion irradiation, Phys. Lett. 380 (2016) 2525.

[39] Z. He, X. Yang, H. Xia, X. Zhou, M. Zhao, Y. Song, T. Wang, Enhancing the ferromagnetization of graphite by successive 12C+ ion implantation steps, Carbon 49 (2011) 1931.

[40] W. Möller, B.M.U. Scherzer, Modeling of hydrogen implantation into graphite, J. Appl. Phys. 64 (1988) 4860.

[41] H.-Y. Guo, C.-C. Ge, M. Xia, L.-P. Guo, J.-H. Chen, Q.-Z. Yan, Effect of helium implantation on SiC and graphite, Chin. Phys. B 24 (2015), 037803.

[42] B.S. Elman, M. Shayegan, M.S. Dresselhaus, H. Mazurek, G. Dresselhaus, Structural characterization of ion-implanted graphite, Phys. Rev. B 25 (1982) 4142.

[43] D.K. Brice, A model of hydrogen implantation into graphite including bulk recombination by tunneling, Nucl. Instrum. Methods Phys. Res. Sect. B Beam Interact. Mater. Atoms 52 (1990) 140.

[44] Y. Gotoh, Interlayer structure changes of graphite after hydrogen ion irradiation, J. Nucl. Mater. 248 (1997) 46.

[45] Y. Gotoh, H. Shimizu, H. Murakami, High resolution electron microscopy of graphite defect structures after KeV hydrogen ion bombardment, J. Nucl. Mater. 162–164 (1989) 851.

[46] S. Hazime, S. Shigemi, G. Yoshitaka, High resolution electron microscopy of graphite defect structures after KeV hydrogen ion bombardment at elevated temperatures, J. Nucl. Mater. 176–177 (1990) 1000.

[47] T. Shi, Q. Peng, Z. Bai, F. Gao, I. Jovanovic, Proton irradiation of graphene: insights from atomistic modeling, Nanoscale 11 (2019) 20754.

[48] P. Willke, J.A. Amani, A. Sinterhauf, S. Thakur, T. Kotzott, T. Druga, S. Weikert, K. Maiti, H. Hofsäss, M. Wenderoth, Doping of graphene by low-energy ion beam implantation: structural, electronic, and transport properties, Nano Lett. 15 (2015) 5110.

[49] U. Bangert, W. Pierce, D.M. Kepaptsoglou, Q. Ramasse, R. Zan, M.H. Gass, J.A. Van den Berg, C.B. Boothroyd, J. Amani, H. Hofsäss, Ion implantation of graphene—toward IC compatible technologies, Nano Lett. 13 (2013) 4902.

[50] F. Watt, M.B.H. Breese, A.A. Bettiol, J.A. van Kan, Proton beam writing, Mater. Today 10 (2007) 20.

[51] W.A. de Heer, C. Berger, M. Ruan, M. Sprinkle, X. Li, Y. Hu, B. Zhang, J. Hankinson, E. Conrad, Large area and structured epitaxial graphene produced by confinement controlled sublimation of silicon carbide, Proc. Natl. Acad. Sci. Unit. States Am. 108 (2011) 16900.

[52] J.F. Ziegler, M.D. Ziegler, J.P. Biersack, SRIM – the stopping and range of ions in matter, Nucl. Instrum. Methods Phys. Res. Sect. B Beam Interact. Mater. Atoms 268 (2010) 1818, 2010.

[53] P.A. Kienzle, B.B. Maranville, K.V. O'Donovan, J.F. Ankner, N.F. Berk, C.F. Majkrzak, Refl1D (2017). https://www.nist.gov/ncnr/reflectometry-software.

[54] A.R. Mazza, A. Miettinen, A.A. Daykin, X. He, T.R. Charlton, M. Conrad, S. Guha, Q. Lu, G. Bian, E.H. Conrad, P.F. Miceli, Revealing interfacial disorder at the growth-front of thick many-layer epitaxial graphene on SiC: a complementary neutron and X-ray scattering investigation, Nanoscale 11 (2019) 14434.

[55] P. Aydogan, E. Arslan, S. Cakmakyapan, E. Ozbay, W. Strupinski, S. Suzer, Voltage contrast X-ray photoelectron spectroscopy reveals graphene-substrate interaction in graphene devices fabricated on the C- and Si- faces of SiC, Appl. Phys. Lett. 107 (2015) 121603.

[56] E. Bekyarova, S. Sarkar, S. Niyogi, M.E. Itkis, R.C. Haddon, Advances in the chemical modification of epitaxial graphene, J. Phys. Appl. Phys. 45 (2012) 154009.

[57] F. Banhart, J. Kotakoski, A.V. Krasheninnikov, Structural defects in graphene, ACS Nano 5 (2011) 26.

[58] J. Petucci, C. LeBlond, M. Karimi, G. Vidali, Diffusion, adsorption, and desorption of molecular hydrogen on graphene and in graphite, J. Chem. Phys. 139 (2013), 044706.

[59] T.L. Makarova, A.L. Shelankov, I.T. Serenkov, V.I. Sakharov, Magnetism in graphite induced by irradiation of hydrogen or helium ions - a comparative study, Phys. Status Solidi B 247 (2010) 2988.

[60] P. Reichart, D. Spemann, A. Hauptner, A. Bergmaier, V. Hable, R. Hertenberger, C. Greubel, A. Setzer, G. Dollinger, D.N. Jamieson, T. Butz, P. Esquinazi, 3D-Hydrogen analysis of ferromagnetic microstructures in proton irradiated graphite, Nucl. Instrum. Methods Phys. Res. Sect. B Beam Interact. Mater. Atoms 249 (2006) 286.

[61] T.L. Makarova, A.L. Shelankov, I.T. Serenkov, V.I. Sakharov, D.W. Boukhvalov, Anisotropic magnetism of graphite irradiated with medium-energy hydrogen and helium ions, Phys. Rev. B 83 (2011), 085417.

[62] O.V. Yazyev, L. Helm, Defect-induced magnetism in graphene, Phys. Rev. B 75 (2007) 125408.